LANGMUIR

Femtosecond Laser-Assisted Top-Restricted Self-Growth Re-Entrant Structures on Shape Memory Polymer for Dynamic Pressure Resistance

Xiangchao Shi,[#] Yachao Zhang,[#] Dong Wu,* Tao Wu, Shaojun Jiang, Yunlong Jiao, Sizhu Wu, Yiyuan Zhang, Yanlei Hu, Weiping Ding,* and Jiaru Chu

Read Online

ACCESS | Metrics & More | Article Recommendations | Supporting Information

ABSTRACT: Bioinspired surface material with re-entrant texture has been proven effective in exhibiting good pressure resistance to droplets with low surface tension under static conditions. In this work, we combined femtosecond laser cutting with shape memory polymer (SMP) and tape to fabricate re-entrant micropillar arrays by proposing a top-restricted self-growth (TRSG) strategy. Our proposed TRSG strategy simplifies the fabrication process and improves the processing efficiency of the re-entrant structure-based surface material. The structural parameters of the re-entrant micropillar array (microdisk diameter D, center-to-center distance P, and height H) can be adjusted through our TRSG processing method. To better characterize the anti-infiltration ability of various re-entrant micropillars, we studied the dynamic process of ethylene glycol droplet deformation by applying external vertical vibration to the surface material. Three parameters (vibration mode, amplitude, and frequency) of the external excitation and structural parameters of the re-entrant micropillar array were systemically investigated. We found that the surface material had better dynamic pressure resistance when P and D of the re-entrant texture were 650 and 500 μm, respectively, after heating for 6 min. This work provides new insights into the preparation and characterization of the surface material, which may find potential applications in microdroplet manipulation, drug testing, and biological sensors.
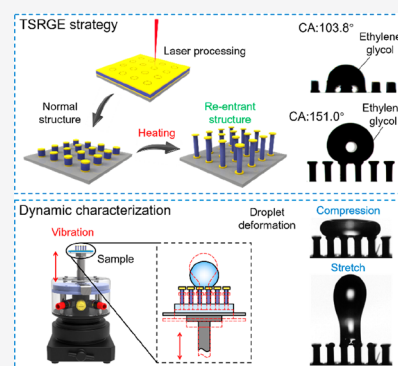
INTRODUCTION

Springtails, small soil-dwelling arthropods, have distinct omniphobic surfaces[1−4] with both static repellency and dynamic pressure resistance, which allow them to survive in complex natural environments. Before the structure surface of springtails was found, researchers have already begun to design re-entrant textures to form functional surface material and predict wetting properties by changing structural parameters.[5−7] Recently, researchers further confirmed that the essential feature of texture surfaces relies on the re-entrant structure that is similar to the springtail's skin. The surface material with re-entrant texture has many potential applications, including self-cleaning,[8−10] liquid transportation,[11,12] drag reduction,[13,14] corrosion prevention,[15] etc. Therefore, various approaches have been proposed to fabricate re-entrant structure-based surface for functional material.[6,7] The mainstream processing method is based on conventional lithography and etching,[16−21] but these processes require additional masks, and the fabricated structures cannot be flexibly adjusted. Moreover, there are other limitations, such as super clean room requirements and chemical reagent pollutions. Recently, two-photon polymerization-based 3D printing technology has been used to fabricate re-entrant texture.[22] Although this is a one-step process, it is time-consuming when realizing large area fabrication.

Bioinspired surface material with re-entrant texture have been proven to be effective in achieving liquid repellence, including antispreading, antiadhesion and antipenetration.[22] Liquid repellence characterization requires different means. The most common means to characterize the antispreading ability is to measure the static contact angle (CA) and sliding angle (SA) of the droplet on the surface.[23−26] Antiadhesion ability can be characterized by contact angle hysteresis (CAH), which was obtained by contacting the droplet with the surface of the structure and then pressing the droplet and pulling it up.[20,21,27,28] Furthermore, by releasing the droplet at different heights above the surface, its impact process on the surface can be observed to characterize the antipenetration ability of the surface.[19,29,30] The common feature of the above-mentioned characterization methods is that the characterized structures remain stationary (Table S1); however, the liquid repellence often occurs in motion scenarios whereas the dynamic
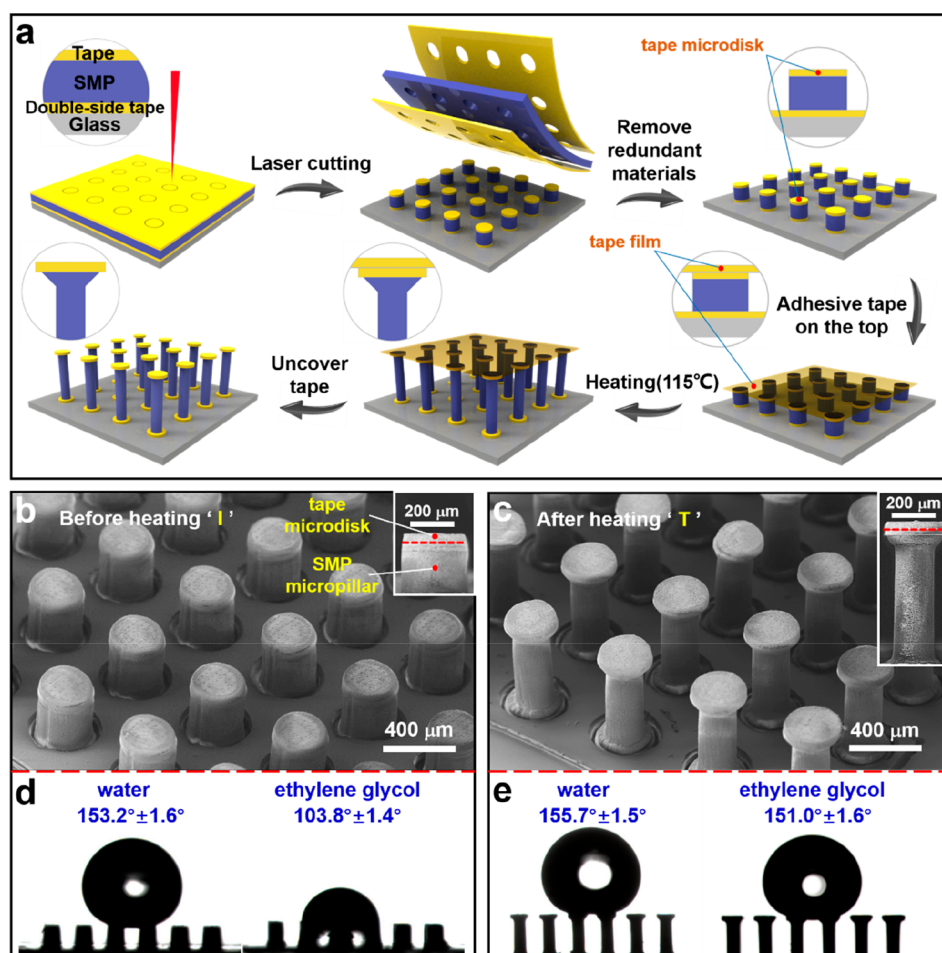
Figure 1. Fabrication of the re-entrant micropillar array and characterization of its hydrophobicity. (a) Schematic illustration of the processing procedure for the re-entrant micropillar array. (b and c) SEM images of two different arrays before and after heating. (b) Axonometric view of the normal micropillar array before heating. The inset shows the front view of a single micropillar before heating. (c) Axonometric view of the re-entrant micropillar array after heating. The inset shows the front view of a single re-entrant micropillar. (d and e) Optical images show CAs of two liquids on two surfaces. (d) The CAs of water and ethylene glycol on the surface of a normal micropillar. The droplet on the surface of the normal micropillar is infiltrated. (e) The CAs of water and ethylene glycol on the surface of the re-entrant micropillar. All of the above droplets are 4 μL in size.

characteristic of liquid repellence in these scenarios is still unclear.

In this work, we first combined femtosecond laser cutting[31−33] with shape memory polymer (SMP) and silicone tape to prepare the surface material with re-entrant texture by utilizing our developed top-restricted self-growth (TRSG) strategy and presented the dynamic characterization of the liquid repellence of the material. Compared with traditional processing methods, the TRSG strategy we proposed simplifies the preparation process and improves the processing efficiency of the surface material with re-entrant texture. It is worth mentioning that the structural parameters of the re-entrant micropillar array (microdisk diameter D, center-to-center distance P, and height H) can be adjusted through our TRSG processing method. We studied the dynamic process of ethylene glycol droplets by applying an external vertical vibration to the surface material. Three parameters (vibration mode, amplitude, and frequency) of external excitation were thoroughly investigated to explore their influences on the anti-infiltration ability of ethylene glycol droplets of the material. The relationship between the anti-infiltration ability with different geometric parameters of the re-entrant texture was

presented. These explorations provide directions for optimizing the surface material to possess a better anti-infiltration ability under motion state. Here, the contribution of the dynamic characterization reflects in two aspects: the first is that this characterization method provides a closer bionic scenario of springtail's resisting droplet infiltration during bouncing process (Figure S1); the second is that the antipenetration mechanism of the re-entrant texture surface under simulated motion state is revealed.

RESULT AND DISCUSSION

Fabrication of Re-Entrant Micropillar Arrays Based on the TRSG Strategy and Characterization of Static Wetting Resistance. The fabrication process of the re-entrant micropillar array (i.e., the re-entrant structure) is illustrated in Figure 1a. The sample consisted of four layers from top to bottom: top tape (Kapton polyimide tape, ∼ 100 μm), heat shrinkable SMP film (Figure S2), double-sided tape, and a glass substrate. First, a circular micropillar array is fabricated by continuous laser scanning and cutting at specific speed (50 mm/s) and energy (300 mw). Figure S3 schematically shows the femtosecond laser galvanometer
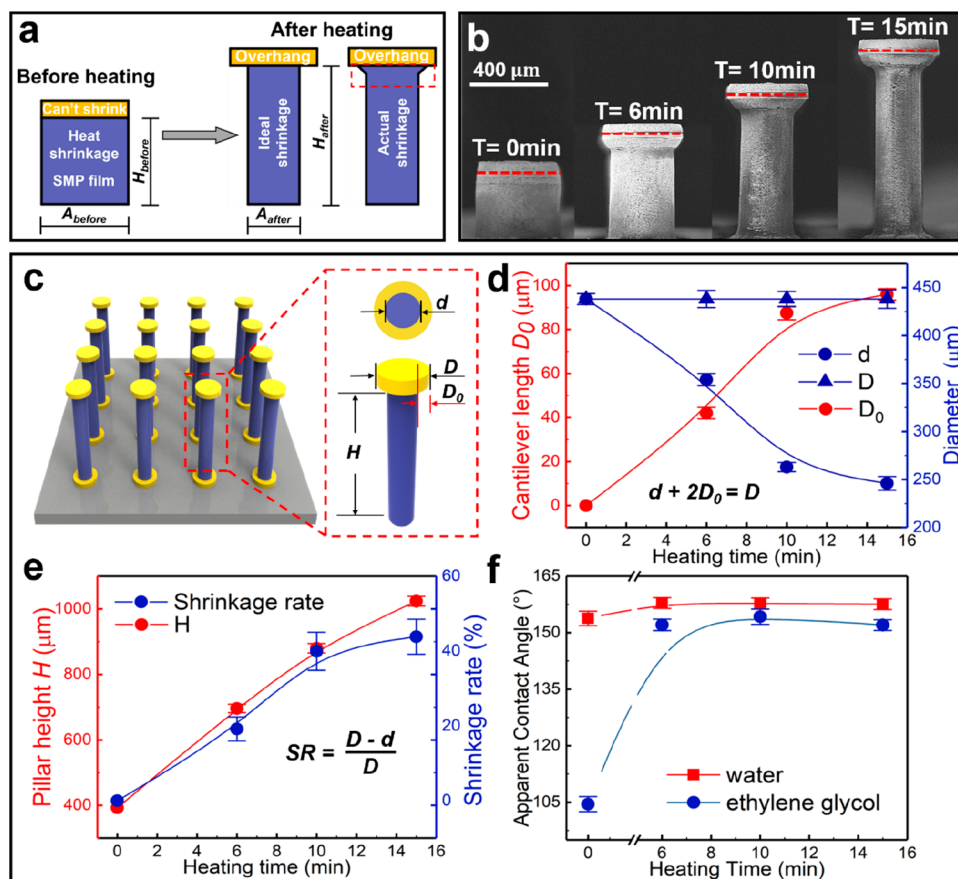
Figure 2. Formation mechanism of the re-entrant structure, and structural parameter characterization. (a) Schematic of the formation mechanism of the re-entrant structure. (b) SEM images of four single micropillars at different heating time, 0, 6, 10, and 15 min. As the heating time increases, the height of the micropillar gradient increases. (c) Schematic of the site used to measure the diameter of the base micropillar d and its height H, the diameter of the top microdisk D and the cantilever length D_0. (d) The quantitative relationship of D, D_0, and d with heating time. (e) The quantitative relationship of H and the shrinkage rate (SR) with the heating time. The calculation of the shrinkage rate is given in the picture. (f) The apparent contact angles of two different liquids (water and ethylene glycol) on the surface of the re-entrant micropillar array with different heating time.

processing system. Then, the redundant material is removed manually with the assistance of a tweezer, leaving the micropillar array on the glass substrate. The SEM of a normal SMP micropillar array with a tape microdisk is shown in Figure 1b. Next, the micropillar array is placed in an oven at 115 °C. Owing to the drastic shrinkage of SMP during heating, a piece of tape film needs to be stuck on the surface of the pillars before heating to ensure that the micropillars grow straight and uniformly (Figure S4). The tape microdisk cannot shrink during the heating process, and a re-entrant micropillar array forms when the tape film is uncovered (Figure 1c).

To characterize the static wetting resistances of the re-entrant micropillar array and the normal micropillar array, 4 μL water and ethylene glycol droplets are deposited. The apparent contact angles of water (γ = 72.8 mN/m) on the re-entrant micropillar array and the normal micropillar array are 155.7° ± 1.5° and 153.2° ± 1.6°, respectively. For lower surface energy liquids, such as ethylene glycol (γ = 47.7 mN/m), the wetting performance is quite different. A spherical ethylene glycol droplet sits on the re-entrant micropillar array (Movie S2) with a contact angle of 151.0° ± 1.5° (Figure 1e), while the droplet infiltrates into the normal micropillar array (Movie S1), exhibiting an apparent contact angle of 103.8° ± 1.4° (Figure 1d). In addition, the difference in apparent contact angle is dominated by the re-entrant structure itself (Figure S5).

We also measured the sliding angle and contact angle hysteresis of water drops (4 μL) on the surfaces of the two arrays. The SAs of the two arrays are 180.0° and 70.5°, respectively. The CAH of the re-entrant micropillar array is 73.5° (Figure S6). Here, an interesting finding is that both the SA and the CA are large, showing rose effect on the surface of the normal micropillar array we fabricated. However, the mechanism on the change of surface adhesion caused by the self-growth process is unclear. Therefore, an intensive study will be performed in the future. In this study, we only focus on the new TRSG strategy for processing the re-entrant structure and the anti-infiltration performance of the re-entrant structure under motion state.

Mechanism of Re-Entrant Structure Formation by Top-Restricted Self-Growth of Heat Shrinkable SMP. In terms of creating re-entrant structures, Kota's group used SMP.[21] Here, we propose a TRSG method with SMP and tape. The mechanism of re-entrant structure formation by top-restricted self-growth of heat shrinkable SMP is systematically investigated (Figure 2a). Before heating, the structure is composed of two materials: the top is a tape microdisk (or PDMS; Figure S7) and the base is a heat shrinkable SMP micropillar. During heating, the size of the base SMP micropillar is reduced in the radial direction due to shrinkage and the micropillar grows higher. Because the top tape
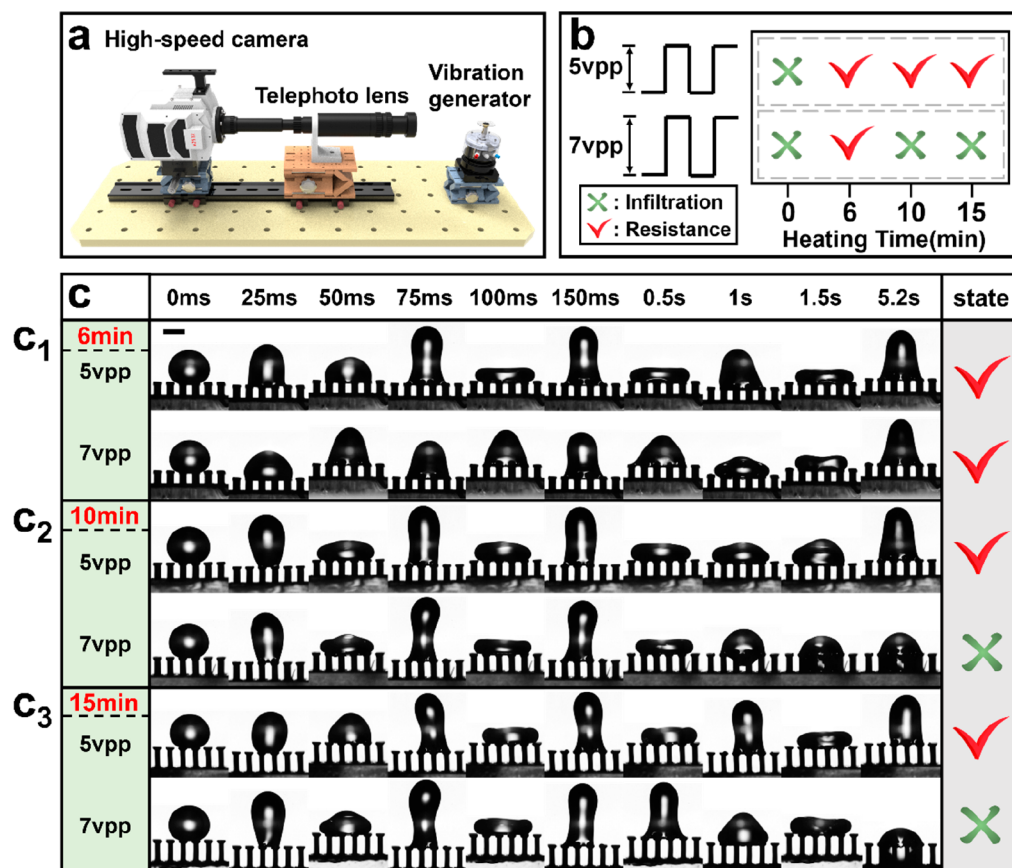
Figure 3. High-speed camera testing system and dynamic characterization of re-entrant structures at different amplitudes. (a) Schematic of the high-speed camera testing system. b) Effect of the heating time and amplitude on the anti-infiltration ability of the re-entrant structure. (c) Snapshots of structures with different heating time, (c_1) 6, (c_2) 10, and (c_3) 15 min, at two different amplitudes (5 and 7 vpp) under a sinusoidal signal. The red and green dotted frames show the ethylene glycol droplet (4 μL) infiltration process of samples heated for 10 and 15 min, respectively. Scale bars: 1 mm.

microdisk cannot shrink while the base SMP can shrink, a re-entrant micropillar forms. Collectively, the shrinkage mismatch of the two different materials in the thermal environment leads to the generation of a re-entrant micropillar. For ideal shrinkage, the base micropillar self-grows uniformly in the height direction, and a perfect "T" shape forms. However, in terms of actual shrinkage, a transition geometric feature between the top tape microdisk and the base SMP micropillar forms. The reason is that during SMP micropillar contraction, the strong adhesive force of the top tape microdisk produces a corresponding shear stress at the interface. The shear stress at the interface between the tape microdisk and the SMP micropillar is largest and decreases with the distance from the longitudinal direction of the SMP micropillar, resulting in the geometric transition feature (Figure S8).

To investigate the restricted self-growing process in detail, micropillars with the same diameters were heated at 115 °C for 0 min (normal micropillar), 6, 10, and 15 min (Figure 2b). As the heating time increases, the diameter of the base micropillar d decreases from 375 to 246 μm and the cantilever length D_0 increases from 32 to 96 μm (Figure 2d). The sites of several structural parameters measured as eigenvalues are schematically shown in Figure 2c. At the same time, the micropillar height H increases from 393 to 1024 μm (the shrinkage rate is calculated in Figure 2e). The static wetting resistance of the fabricated re-entrant micropillar array is characterized by measuring the apparent contact angle on the surface (Figure

2f). The CAs of water at different heating time are 153.8° ± 1.2°, 157.9° ± 1.4°, 157.7° ± 1.5°, and 157.6° ± 1.4°; the CAs of ethylene glycol at different heating time are 104.5° ± 1.4°, 152.1° ± 1.5°, 154.2° ± 2.1°, and 152.0° ± 1.4° (the measured values can be expected by the Cassie−Baxter theory[34−39]). When the heating time is 0 min, the re-entrant micropillar has not yet formed, and the poor liquid repellency of the normal micropillar cannot resist ethylene glycol infiltration (the local geometric angle of the normal micropillar is −90°[2]). When the heating time exceeds 6 min (including 6 min), the re-entrant micropillar forms. However, there is almost no difference in CA (static wetting performance) between structures with different heating time. Although the micropillars grow higher as the heating time increases, the center-to-center distance of the micropillars and the duty cycle of the array remain unchanged because the top tape cannot shrink (Figure S9). In addition, the local geometric angle[37,40] of the re-entrant micropillar is 0° and remains unchanged during heating process (Figure S10).

Effects of the Signal Amplitudes on the Anti-Infiltration Abilities of the Surface Material with Re-Entrant Texture for Different Heights. Since the static contact angle is unable to precisely characterize the liquid repellence of the re-entrant structure, the dynamic characterization (i.e., in situ vibration test) is performed to distinguish the anti-infiltration ability of re-entrant structures with
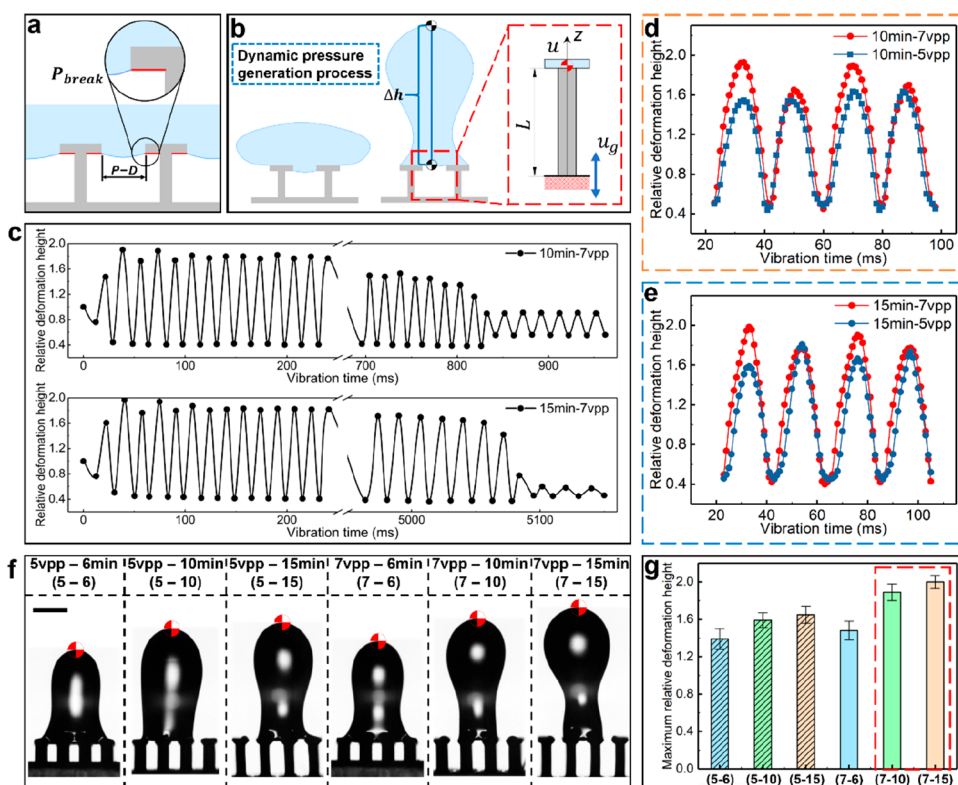
Figure 4. Explanation of the mechanism of droplet infiltration under external vibration. (a) Breakthrough pressure of the re-entrant structure (P_{break}). The P_{break} values are the same for structures with the same geometric parameters pair $\{P, D\}$. (b) Dynamic pressure caused by droplet deformation. The vibration process of the structure can be described by a simplified vibration mechanics model. (c) Relationship between the relative deformation height of the droplet and the vibration time under fixed amplitude (7 vpp) for structures heated at 10 and 15 min. The relative deformation height is defined as the ratio of the current droplet height to the initial droplet height. (d) Comparison of the relative deformation heights in local periods for the re-entrant structure after heating for 10 min. (e) Comparison of the relative deformation heights in local periods for the re-entrant structure after heating for 15 min. (f) Snapshots of the maximum deformation position of droplets at two amplitudes (5 and 7 vpp) for structures with different heating time (6, 10, and 15 min). Scale bars: 1 mm. (g) Statistical histogram of the maximum relative deformation height. Columns of the same color represent structures heated for the same time, and different patterns represent different amplitudes.

different heights (actually, the deformation of droplets also can reflect the strong pinning of the contact line).

The testing system is schematically shown in Figures 3a and S11. The sample is placed on the vibration generator, and a high-speed camera or CCD monitors the dynamic process of the droplet on the surface of the re-entrant micropillar array under vibration. The ability to resist the penetration of ethylene glycol droplets (4 μL) is characterized. These re-entrant micropillar arrays heated at 0, 6, 10, and 15 min have the same plane geometric design parameters (the diameter of the microdisk is 500 μm and the center-to-center distance is 650 μm). Excitation (square wave, 60 Hz) is generated by a vibration generator controlled by the signal generator. Two different amplitudes (5 vpp, 7 vpp, which represent the amplitudes are 180 ± 5 μm and 250 ± 5 μm, respectively) are applied in the test (the voltage-amplitude conversion curve is shown in Figure S12). Figure 3b shows the influences of the heating time and amplitude on the anti-infiltration ability of different microstructures. The droplet easily penetrates into the normal micropillar array (0 min) at 5 vpp and 7 vpp. At the lower amplitude (5 vpp), the droplet cannot penetrate into the re-entrant micropillar array. At the higher amplitude (7 vpp), the droplet penetrates into the 10 and 15 min samples but cannot penetrate into the 6 min samples. A series of time-sequence images of the droplet on samples (6, 10, and 15 min) under vibration are captured by a high-speed camera (Figure

3c$_1$,c$_2$,c$_3$ and Movies S3 and S4). The difference in liquid repellence of structures with different heating time cannot be distinguished by static contact angles but can be distinguished by the anti-infiltration performance under dynamic conditions.

Mechanism of Ethylene Glycol Droplet Infiltration on the Surface of Re-Entrant Structure under External Vertical Vibration. The results of the vibration test presented in Figure 3 show that the re-entrant structure heated for 6 min has better dynamic pressure resistance than that of those heated for 10 and 15 min. The reason for the difference is discussed in Figure 4. The breakthrough pressure depends on structure shape.[5,41] For the re-entrant structure we developed, the breakthrough pressure (P_{break}) can be described as follows:[4]

$$P_{break} = \frac{4\gamma \sin(\theta_Y + \psi)}{P - D} \qquad (1)$$

where ψ is the local geometric angle, γ is the interfacial energy of the liquid–gas phase boundary, θ_Y is the intrinsic contact angle, and P and D are the center-to-center distance and the microdisk diameter of re-entrant structures, respectively. Since the local geometric angle of the re-entrant structure is 0°, eq 1 can be simplified to the following formula[2] (Figure 4a):
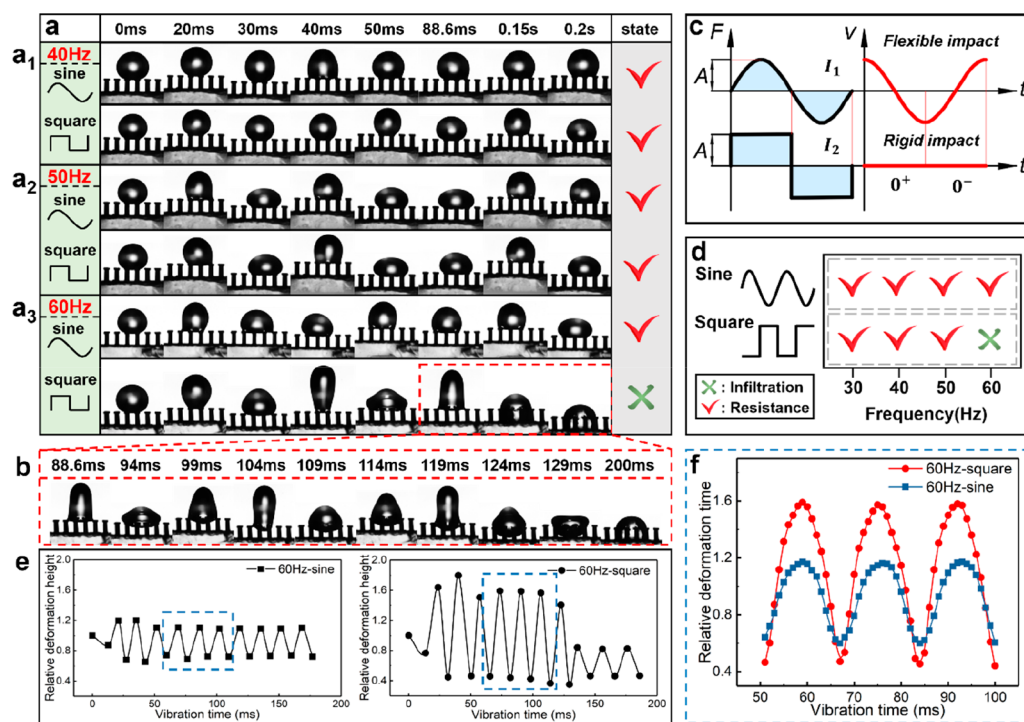
Figure 5. Characterization of the structural dynamic stability with the frequency and vibration mode of the signal. (a) Snapshots captured in the vibration test by a high-speed camera of different signals at specific frequencies, (a_1) 40, (a_2) 50, and (a_3) 60 Hz. The red dotted frame shows the process of infiltration. (b) Unfolded time-sequence images of the red dotted frames of the infiltration process. (c) Principle explanation for the different physical characteristics of the sinusoidal wave signal and square wave signal. (d) Effect of the frequencies and vibration modes on the anti-infiltration ability of the re-entrant structure. (e) Relationship between the relative deformation height and vibration time of droplets with two modes (square, sine) at 60 Hz. (f) Comparison of the relative deformation heights in local periods under two vibration modes at 60 Hz.

$$P_{break} = \begin{cases} \dfrac{4\gamma \sin \theta_Y}{P - D}, & \theta_Y \le 90° \\[3mm] \dfrac{4\gamma}{P - D}, & \theta_Y > 90° \end{cases} \tag{2}$$

The intrinsic contact angle of the ethylene glycol droplet on the silicone tape is $100.5° \pm 2.7°$ (Figure S13). Thus, eq 2 can be further simplified as follows:

$$P_{break} = \frac{4\gamma}{P - D} \tag{3}$$

Equation 3 shows that when the geometric design parameter pair $\{P, D\}$ of the re-entrant structure is the same, P_{break} is invariant for the same droplets. Therefore, we believe that the generation of droplet infiltration is related to the deformation height (Δh) of droplets during the vibration process. Under a given base displacement (u_g), the droplet deforms and generates dynamic pressure (Figure 4b). Once the dynamic pressure (P_H) generated by the droplet is greater than P_{break}, the droplet will infiltrate. We define this relationship as the infiltration condition, which is expressed as follows:

$$P_H = \frac{1}{2}\rho v^2 > \frac{4\gamma}{P - D} = P_{break} \tag{4}$$

where ρ and v denote the liquid density and the contact point velocity, respectively. By monitoring the high-speed camera, we can find the difference of Δh with different structure heights, which is controlled by different heating time (10 min, 15 min) at fixed amplitudes (7 vpp) during the entire vibration process (Figure 4c). Here, in order to eliminate the statistical error of the deformation height caused by the difference in droplet size,

the droplet deformation height is replaced by the relative deformation height, which is defined as the ratio of the current droplet height to the initial droplet height. The relationship between the relative deformation height and vibration time for 5 vpp is shown in Figure S14. Local periods aligned with the same time scale (1 ms interval) are compared (Figure 4d,e). We can see that the higher the structure and the larger the amplitude of external vibration, the greater the deformation degree of droplets according to the statistical results presented in Figure 4g. The statistical results are obtained from snapshots of the droplet maximum deformation position (Figure 4f). Here, the contact point velocity v is approximately expressed as the sum of the base velocity and the droplet deformation velocity (the droplet deformation velocity can be calculated from the height profiles). The calculated contact point velocities are 1.06, 1.17, 1.20, 1.36, 1.55, and 1.57 m/s for operating conditions 6 min-5vpp, 10 min-5vpp, 15 min-5vpp, 6 min-7vpp, 10 min-7vpp, and 15 min-7vpp, respectively.

We use mechanical vibration theory to explain why droplet deformation increases with increasing structure height. A single re-entrant micropillar under vibration conditions can be simplified to a beam fixed at one end with base displacement u_g (Figure 4b). According to theoretical mechanics, the deformation of the droplet is positively correlated with the displacement of the contact point between the droplet and the micropillar, that is, free-end displacement u. Given the base displacement, the free-end displacement can be solved by the following formula:[42]

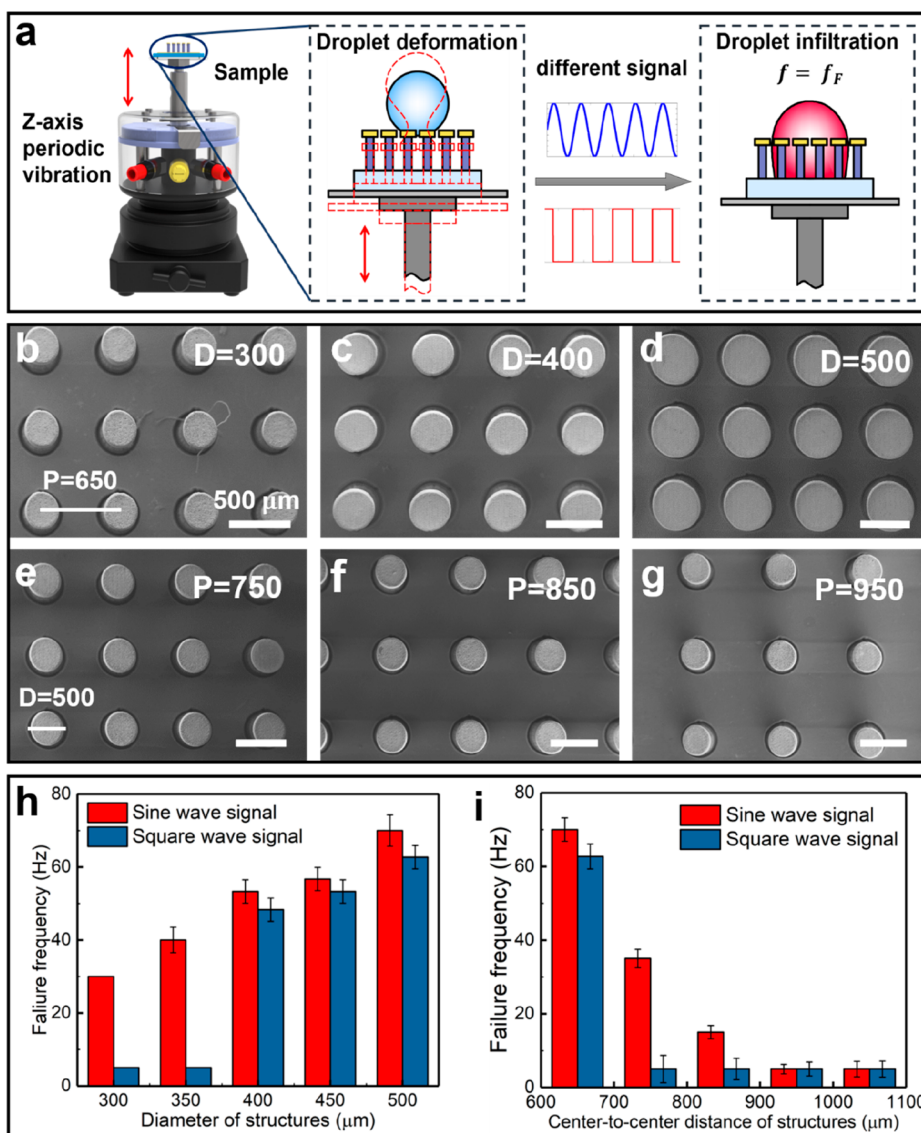$$u = \left(1 + \frac{16\rho_s l^2 \omega^2}{\pi^3 E}\right) u_g \tag{5}$$

Figure 6. Failure frequency measurements of re-entrant micropillar arrays with different structural parameters. (a) Schematic of the vibration testing process. (b−d) SEM images of re-entrant micropillar arrays with a fixed center-to-center distance and increased diameters. The diameters are 300, 400, and 500 μm, respectively. (e−g) SEM images of re-entrant micropillar arrays with fixed diameters and increased center-to-center distances. The center-to-center distances are 750, 850, and 950 μm, respectively. (h) Relationship between the failure frequencies and structure diameters for two different signals. (i) Relationship between the failure frequencies and center-to-center distance of structures for two different signals.

where ρ_s, l, and E represent the density, length, and elastic modulus of the re-entrant micropillar material, respectively. The given u_g is

$$u_g = \begin{cases} A, & kT \leq t < \left(k + \dfrac{1}{2}\right)T \\[2ex] -A, & \left(k + \dfrac{1}{2}\right)T \leq t < (k+1)T \end{cases} \qquad (6)$$

where A and T denote the amplitude and period of the square wave, respectively, k is an integer which greater than or equal to zero. By combining eq 5 with eq 6, it is obvious that the free-end displacement increases with the increasing pillar height and signal amplitude.

The dynamic pressure (deformation) of the droplet increases as the pillar height (the heating time) increases. When the heating time exceeds a certain threshold between 6

and 10 min (eq 4), the droplet will infiltrate (Figure 3c). It should be noted that the infiltration occurrence and the infiltration speed are unrelated. That is, for the situation of droplet infiltration, even if the deformation height of the droplet is positively related to the pillar height, it does not mean that the bigger deformed droplets will infiltrate faster (Figure 3c). In fact, the infiltration speed depends on many factors, such as surface topology, base inclination, and status of the three-phase contact line under vibration; thus, it is very difficult to predict the infiltration speed of the droplet.

For the ethylene glycol droplets on the re-entrant structure, the theoretically calculated P_{break} is approximately 1272 pa ($P = 650$ μm, $D = 500$ μm, $\gamma = 47.7$ mN/m) and the theoretically calculated values of P_H are 625.7, 764.0, 799.7, 1037.3, 1343.7, and 1376.8 Pa, corresponding to operating conditions 6 min-5vpp, 10 min-5vpp, 15 min-5vpp, 6 min-7vpp, 10 min-7vpp, and 15 min-7vpp, respectively. The calculated results are in

consistence with the phenomena presented in experiments (Figure 3c). That is, when $P_{break} < P_H$, the infiltration occurs.

Influence of the Specific Two Signal Modes on the Anti-Infiltration Ability of the Surface Material with Re-Entrant Texture. The influence of the frequencies and vibration modes are investigated (Figure 5). The samples are heated for 10 min, and the amplitude of the external vibration is fixed at 7 vpp. High-speed camera images for vibration tests under two kinds of excitation (sine and square waves) with varied frequencies (40, 50, and 60 Hz) are captured (Figures 5a$_1$,a$_2$,a$_3$ and Movie S5 and S6). At 40 and 50 Hz, droplets cannot infiltrate under the two different vibration modes, and the microstructure shows good anti-infiltration ability. When the frequency increases to 60 Hz, the droplet under the square wave signal begins to infiltrate. The details of the infiltration process are shown in Figure 5b. The entire infiltration process lasts for 40.4 ms from the beginning of infiltration to full contact with the substrate. The deformation height of the droplet throughout the vibration process and magnified images of local periods (1 ms interval) are recorded (Figure 5e,f). In contrast to the steady noninfiltrating phenomenon of the droplet under the sinusoidal signal, we believe that the process is caused by the different characteristics of the two signals. Figure 5c shows the difference between sine and square wave signals. On the one hand, considering the variations of the two forces produced by these two signals, we can see that the impulse of square wave signal I_1 is larger than that of sine signal I_2 (sum of area) in one period, that is, the momentum change rate is larger. On the other hand, compared with the rigid impact brought by the square signal, the speed of flexible impact caused by the sine signal has no abrupt change. The above two factors explain why the droplets are more likely to infiltrate under the square wave signal. The results of the horizontal comparison of each row reveal that when the frequency increases to a certain value, the droplet on the surface of the re-entrant micropillar array changes from the resistant state to the infiltrated state (Figure 5d). The higher the failure frequency (f_F) is, the better the anti-infiltration ability is. Collectively, the vibration frequency and vibration mode affect the antipenetration of the re-entrant structure significantly.

Effect of Plane Geometric Design Parameters on the Anti-Infiltration Ability under Motion State. We further explore the influence of the plane geometric design parameters on the f_F, that is, the influence of the structural geometric parameters on the anti-infiltration ability under two different vibration modes (Figure 6a). A series of re-entrant micropillar arrays (heating 10 min) are fabricated by changing the geometric parameters of the laser-scanning path. Here, we define two different sets of structural parameters: the center-to-center distance P in one group of re-entrant structures is fixed and the diameter D of the other group is fixed (Figure S15). In the first set of structures, P is fixed at 650 μm and D is increased from 300 to 500 μm in increments of 50 μm. In the second set, D is fixed at 500 μm and P is increased from 650 to 1050 μm in increments of 100 μm (SEM images are shown in Figure 6b−g). Figure 6h shows the relationship between f_F and D for square and sinusoid waves with the amplitude 5 vpp. Figure 6i shows the relationship between f_F and P for the two waves. From the measurements, we can see that the f_F increases with D and decreases with P. This finding can be explained by the change of P_{break} with the geometric parameters P and D (eq 3). For the same droplets, since the

local geometric angle ψ of the re-entrant structure is 0°, P_{break} is mainly affected by P and D. For a constant P, once D increases, P_{break} increases; that is, the droplets are more difficult to infiltrate. Conversely, when D is constant, once P increases, P_{break} decreases, indicating that the droplets are easy to infiltrate. Here, the qualitative relationship between P_{break} and P, D (eq 3) is consistent with the conclusion in the literature,[43] providing a direction to optimize structural parameters with better anti-infiltration properties under dynamic conditions.

■ CONCLUSION

In summary, we combined femtosecond laser cutting with SMP and tape to prepare surface material with re-entrant texture by proposing our developed top-restricted self-growth (TRSG) strategy. Compared with traditional processing methods, our proposed TRSG strategy simplifies the preparation process and improves the processing efficiency of the material. The diameter, center-to-center distance, height and cantilever length can be adjusted through the flexibility of our TRSG processing method. We further studied the dynamic process of ethylene glycol droplet deformation by applying external vertical vibration to the surface material. After exploring the effects of three parameters (amplitude, vibration mode, frequency) of external excitation, we found that large amplitudes and frequencies make the droplets more susceptible to infiltration. At the same time, the square wave signal, as a rigid impact, has the same promotion effect on droplet infiltration. However, the height of the micropillar actually affects the infiltration process. Shorter structure (6 min) has better anti-infiltration ability because droplets deform less on its surface; this phenomenon can be explained by the theory of vibration mechanics (i.e., the deduced infiltration condition between breakthrough pressure and dynamic pressure). Finally, by exploring the relationship between the failure frequency and structural parameters, we concluded that increasing D and decreasing P are helpful for improving the anti-infiltration performance of the surface material. The unique prepare method and dynamic vibration testing technique not only provides new insights into the preparation and characterization of the bioinspired re-entrant structure-based surface material but also can be used for other biomimetic functional material, which may further promote their practical applications.

■ EXPERIMENTAL DETAILS

Materials. The SMP used in this study is a kind of prestretched polystyrene film, in sheet form (thickness: 300 μm), that was purchased from Dongguan Nogard Arts & Crafts Factory. We cut the SMP film into small pieces (12 × 8 mm) and pasted it on small laboratory slides (20 × 15 mm) with double-sided tape (Kapton, TED PELLA, Inc., U.S.A.) to prepare the samples for subsequent processing. The chemical composition of the adhesion tape is silicone (γ = 18−22 mN/m).

Femtosecond Laser Fabrication Method. A regenerative amplified Ti:sapphire femtosecond laser system (Legend Elite-1K-HE, Coherent, U.S.A.) with a 104 fs pulse width, 1-kHz repetition rate, and 800 nm central wavelength was employed to fabricate microstructures on the polystyrene film. The linearly polarized laser beam was guided onto the surface of the polystyrene film by a galvoscanner system (SCANLAB, Germany) equipped with a telecentric f-theta lens with a focal length of 63 mm. A Z-axis mobile platform (THORLABS, U.S.A.) was adjusted to ensure that the laser focused on the surface of the sample. The diameter of the focused spot was approximately 20 μm. The scanning path (circular

geometry) was drawn by AutoCAD 2016 (Autodesk, U.S.A.) and saved as a dxf 2013 file. Then, the dxf file was imported into the processing software (Samlight). The scanning sequence was the same as the drawing sequence and could also be changed. The pulse energy (300 mw) was adjusted by using a combination of a half-wave plate and a low dispersion polarizer. The scanning speed (50 mm/s) and scanning times (380) were controlled by the software Samlight. A low-power (50 mW) laser was used to generate rough microstructures on top of the microdisk to reduce the adhesive area with tape for easier stripping.

Heating Process. After laser cutting, a normal micropillar array was achieved. Then, the pretreated sample was placed in an oven (Thermo Fisher Scientific, U.S.A.) at 115 °C to form a re-entrant micropillar array. The height of the re-entrant micropillar array can be accurately adjusted by changing the heating time. In this work, we have selectively set three heating time of 6, 10, and 15 min.

Dynamic Stability Characterization Experiment. Ethylene glycol droplets ($\sim$4 μL) were deposited on the surface of the structure, and the stability of the surface was evaluated by the infiltration state of the droplets. A vibration generating device (vibration generator No. 2185, Frederiksen, Denmark) was used to generate mechanical vibration. The vibration generator was connected to a signal generator (RIGOL DG2041A, China). A high-speed camera (Phantom v2512, U.S.A.) was used to capture the shape of the droplets at high frequencies under vibration. The parameters were set as follows: frame number, 10 000 fps; exposure time, 50 μs; and magnification, 3.2.

Structure and Hydrophobic Characterizations. The microstructure of the re-entrant micropillar array was characterized by a secondary scanning electron microscope (Zeiss EVO18, Germany) with an accelerating voltage of 10 kV. A CCD (Mindvision, China) with a macro lens was used to record the vibration process of the micropillar interface. The CAs were measured by using a contact angle system (CA100D, Innuo, China) with 4 μL droplets (water and ethylene glycol) on the as-prepared samples under 10% relative humidity and 20 °C temperature.

ASSOCIATED CONTENT

Supporting Information

The Supporting Information is available free of charge at https://pubs.acs.org/doi/10.1021/acs.langmuir.0c02335.

> (1) A table (Table S1) showing comparison of characterization methods; (2) a figure (Figure S1) showing the scenario of springtail's resisting droplet infiltration during bouncing process; a figure (Figure S2) showing the characterization of the heat-shrinkage property of a polystyrene film; a figure (Figure S3) showing the schematic of the femtosecond laser galvanometer processing system; a figure (Figure S4) showing the comparison of re-entrant micropillar arrays with and without top tape; a figure (Figure S5) showing the comparison of the wettability between the surfaces of two structures with ethylene glycol droplets; a figure (Figure S6) showing SA and CAH of pillar and re-entrant structures; a figure (Figure S7) showing the re-entrant micropillar structure fabricated with shape memory polymer and polydimethylsiloxane; a figure (Figure S8) showing the formation mechanism of the transition geometric feature during the heating process; a figure (Figure S9) showing SEM images of re-entrant micropillar arrays; a figure (Figure S10) showing the local geometric angles of re-entrant structures during heating process; a figure (Figure S11) showing the schematic of the vibration testing system; a figure (Figure S12) showing the voltage-amplitude conversion curve; a figure (Figure S13) showing the intrinsic

contact angle of silicone tape without processing; a figure (Figure S14) showing the relationship between relative deformation height and vibration time for the structure heated for 10 min under 5 vpp amplitude; a figure (Figure S15) showing structures with two sets of different structural parameters, structures with two sets of different design parameters (PDF)

> Video (Movie S1) showing the unheated sample with a normal pillar structure that ethylene glycol droplets can easily infiltrate (MP4)

> Video (Movie S2) showing the sample heated at 115 °C for 10 min with a re-entrant structure that ethylene glycol droplets cannot infiltrate (MP4)

> Video (Movie S3) showing the ethylene glycol droplet vibration process on the surface of re-entrant micropillar arrays heated for different time (6 min, 10 and 15 min) under a given amplitude (5 vpp) (MP4)

> Video (Movie S4) showing the ethylene glycol droplet vibration process on the surface of re-entrant micropillar arrays heated for different time (6 min, 10 and 15 min) under a given amplitude (7 vpp) (MP4)

> Video (Movie S5) showing the ethylene glycol droplet vibration process on the surface of the re-entrant micropillar array at different frequencies (40 Hz, 50 and 60 Hz) under sine waves (MP4)

> Video (Movie S6) showing the ethylene glycol droplet vibration process on the surface of the re-entrant micropillar array at different frequencies (40 Hz, 50 and 60 Hz) under square waves (MP4)

AUTHOR INFORMATION

Corresponding Authors

Dong Wu − *CAS Key Laboratory of Mechanical Behaviour and Design of Materials, Key Laboratory of Precision Scientific Instrumentation of Anhui Higher Education Institutes, Department of Precision Machinery and Precision Instrumentation, University of Science and Technology of China, Hefei 230026, China;* orcid.org/0000-0003-0623-1515; Email: dongwu@ustc.edu.cn

Weiping Ding − *Department of Electronic Science and Technology, University of Science and Technology of China, Hefei 230026, China;* orcid.org/0000-0002-3331-1011; Email: wpdings@ustc.edu.cn

Authors

Xiangchao Shi − *Department of Electronic Science and Technology, University of Science and Technology of China, Hefei 230026, China*

Yachao Zhang − *CAS Key Laboratory of Mechanical Behaviour and Design of Materials, Key Laboratory of Precision Scientific Instrumentation of Anhui Higher Education Institutes, Department of Precision Machinery and Precision Instrumentation, University of Science and Technology of China, Hefei 230026, China*

Tao Wu − *Department of Modern Mechanics, University of Science and Technology of China, Hefei 230026, China;* orcid.org/0000-0002-0291-6595

Shaojun Jiang − *CAS Key Laboratory of Mechanical Behaviour and Design of Materials, Key Laboratory of Precision Scientific Instrumentation of Anhui Higher Education Institutes, Department of Precision Machinery and Precision Instrumentation, University of Science and Technology of China, Hefei 230026, China*

Yunlong Jiao − *Institute of Tribology, Hefei University of Technology, Hefei 230009, China;* ◉ orcid.org/0000-0001-7718-7342

Sizhu Wu − *School of Instrument Science and Optoelectronics Engineering, Hefei University of Technology, Hefei 230009, China*

Yiyuan Zhang − *CAS Key Laboratory of Mechanical Behaviour and Design of Materials, Key Laboratory of Precision Scientific Instrumentation of Anhui Higher Education Institutes, Department of Precision Machinery and Precision Instrumentation, University of Science and Technology of China, Hefei 230026, China*

Yanlei Hu − *CAS Key Laboratory of Mechanical Behaviour and Design of Materials, Key Laboratory of Precision Scientific Instrumentation of Anhui Higher Education Institutes, Department of Precision Machinery and Precision Instrumentation, University of Science and Technology of China, Hefei 230026, China;* ◉ orcid.org/0000-0003-1964-0043

Jiaru Chu − *CAS Key Laboratory of Mechanical Behaviour and Design of Materials, Key Laboratory of Precision Scientific Instrumentation of Anhui Higher Education Institutes, Department of Precision Machinery and Precision Instrumentation, University of Science and Technology of China, Hefei 230026, China;* ◉ orcid.org/0000-0001-6472-8103

Complete contact information is available at:
https://pubs.acs.org/10.1021/acs.langmuir.0c02335

Author Contributions

[#]X.S. and Y.Z. contributed equally to this work.

Notes

The authors declare no competing financial interest.

■ REFERENCES

(1) Helbig, R.; Nickerl, J.; Neinhuis, C.; Werner, C. Smart Skin Patterns Protect Springtails. *PLoS One* **2011**, *6* (9), e25105.

(2) Hensel, R.; Helbig, R.; Aland, S.; Braun, H. G.; Voigt, A.; Neinhuis, C.; Werner, C. Wetting Resistance at Its Topographical Limit: The Benefit of Mushroom and Serif T Structures. *Langmuir* **2013**, *29* (4), 1100−1112.

(3) Hensel, R.; Helbig, R.; Aland, S.; Voigt, A.; Neinhuis, C.; Werner, C. Tunable nano-replication to explore the omniphobic characteristics of springtail skin. *NPG Asia Mater.* **2013**, *5*, e37.

(4) Hensel, R.; Neinhuis, C.; Werner, C. The springtail cuticle as a blueprint for omniphobic surfaces. *Chem. Soc. Rev.* **2016**, *45* (2), 323−341.

(5) Tuteja, A.; Choi, W.; Mabry, J. M.; McKinley, G. H.; Cohen, R. E. Robust omniphobic surfaces. *Proc. Natl. Acad. Sci. U. S. A.* **2008**, *105* (47), 18200−18205.

(6) Tuteja, A.; Choi, W.; Ma, M. L.; Mabry, J. M.; Mazzella, S. A.; Rutledge, G. C.; McKinley, G. H.; Cohen, R. E. Designing superoleophobic surfaces. *Science* **2007**, *318* (5856), 1618−1622.

(7) Tuteja, A.; Choi, W. J.; McKinley, G. H.; Cohen, R. E.; Rubner, M. F. Design parameters for superhydrophobicity and super-oleophobicity. *MRS Bull.* **2008**, *33* (8), 752−758.

(8) Kim, D.; Im, H.; Kwak, M. J.; Byun, E.; Im, S. G.; Choi, Y. K. A Superamphiphobic Sponge with Mechanical Durability and a Self-Cleaning Effect. *Sci. Rep.* **2016**, *6*, 29993.

(9) Jung, Y. C.; Bhushan, B. Dynamic Effects Induced Transition of Droplets on Biomimetic Superhydrophobic Surfaces. *Langmuir* **2009**, *25* (16), 9208−9218.

(10) Lu, Y.; Sathasivam, S.; Song, J. L.; Crick, C. R.; Carmalt, C. J.; Parkin, I. P. Robust self-cleaning surfaces that function when exposed to either air or oil. *Science* **2015**, *347* (6226), 1132−1135.

(11) Li, J.; Qin, Q. H.; Shah, A.; Ras, R. H. A.; Tian, X. L.; Jokinen, V. Oil droplet self-transportation on oleophobic surfaces. *Sci. Adv.* **2016**, *2* (6), e1600148.

(12) Han, H.; Lee, J. S.; Kim, H.; Shin, S.; Lee, J.; Kim, J.; Hou, X.; Cho, S. W.; Seo, J.; Lee, T. Single-Droplet Multiplex Bioassay on a Robust and Stretchable Extreme Wetting Substrate through Vacuum-Based Droplet Manipulation. *ACS Nano* **2018**, *12* (2), 932−941.

(13) Zhang, S. S.; Ouyang, X.; Li, J.; Gao, S.; Han, S. H.; Liu, L. H.; Wei, H. Underwater Drag-Reducing Effect of Superhydrophobic Submarine Model. *Langmuir* **2015**, *31* (1), 587−593.

(14) Lee, C.; Kim, C. J. Underwater Restoration and Retention of Gases on Superhydrophobic Surfaces for Drag Reduction. *Phys. Rev. Lett.* **2011**, *106* (1), 014502.

(15) Wen, N.; Peng, S.; Yang, X. J.; Long, M. Y.; Deng, W. S.; Chen, G. Y.; Chen, J. Q.; Deng, W. L. A Cycle-Etching Approach Toward the Fabrication of Superamphiphobic Stainless Steel Surfaces With Excellent Anticorrosion Properties. *Adv. Eng. Mater.* **2017**, *19* (6), 1600879.

(16) Hensel, R.; Finn, A.; Helbig, R.; Braun, H. G.; Neinhuis, C.; Fischer, W. J.; Werner, C. Biologically Inspired Omniphobic Surfaces by Reverse Imprint Lithography. *Adv. Mater.* **2014**, *26* (13), 2029−2033.

(17) Lee, S. E.; Kim, H. J.; Lee, S. H.; Choi, D. G. Super-amphiphobic Surface by Nanotransfer Molding and Isotropic Etching. *Langmuir* **2013**, *29* (25), 8070−8075.

(18) Grigoryev, A.; Roiter, Y.; Tokarev, I.; Luzinov, I.; Minko, S. Colloidal Occlusion Template Method for Micromanufacturing of Omniphobic Surfaces. *Adv. Funct. Mater.* **2013**, *23* (7), 870−877.

(19) Yun, G. T.; Jung, W. B.; Oh, M. S.; Jang, G. M.; Baek, J.; Kim, N. I.; Im, S. G.; Jung, H. T. Springtail-inspired superomniphobic surface with extreme pressure resistance. *Sci. Adv.* **2018**, *4* (8), eaat4978.

(20) Kim, J. H.; Shim, T. S.; Kim, S. H. Lithographic Design of Overhanging Microdisk Arrays Toward Omniphobic Surfaces. *Adv. Mater.* **2016**, *28* (2), 291−298.

(21) Wang, W.; Salazar, J.; Vahabi, H.; Joshi-Imre, A.; Voit, W. E.; Kota, A. K. Metamorphic Superomniphobic Surfaces. *Adv. Mater.* **2017**, *29* (27), 1700295.

(22) Liu, X. J.; Gu, H. C.; Wang, M.; Du, X.; Gao, B. B.; Elbaz, A.; Sun, L. D.; Liao, J. L.; Xiao, P. F.; Gu, Z. Z. 3D Printing of Bioinspired Liquid Superrepellent Structures. *Adv. Mater.* **2018**, *30* (22), 1870157.

(23) Choi, J.; Jo, W.; Lee, S. Y.; Jung, Y. S.; Kim, S. H.; Kim, H. T. Flexible and Robust Superomniphobic Surfaces Created by Localized Photofluidization of Azopolymer Pillars. *ACS Nano* **2017**, *11* (8), 7821−7828.

(24) Chen, C.; Huang, Z. C.; Jiao, Y. L.; Shi, L. A.; Zhang, Y. Y.; Li, J. W.; Li, C. Z.; Lv, X. D.; Wu, S. Z.; Hu, Y. L.; Zhu, W. L.; Wu, D.; Chu, J. R.; Jiang, L. In Situ Reversible Control between Sliding and Pinning for Diverse Liquids under Ultra-Low Voltage. *ACS Nano* **2019**, *13* (5), 5742−5752.

(25) Wang, Q. B.; Xu, B. J.; Hao, Q.; Wang, D.; Liu, H.; Jiang, L. In situ reversible underwater superwetting transition by electrochemical atomic alternation. *Nat. Commun.* **2019**, *10*, 09201.

(26) Yang, Y.; Li, X. J.; Zheng, X.; Chen, Z. Y.; Zhou, Q. F.; Chen, Y. 3D-Printed Biomimetic Super-Hydrophobic Structure for Micro-droplet Manipulation and Oil/Water Separation. *Adv. Mater.* **2018**, *30* (9), 1870062.

(27) Liu, M. J.; Wang, S. T.; Wei, Z. X.; Song, Y. L.; Jiang, L. Bioinspired Design of a Superoleophobic and Low Adhesive Water/Solid Interface. *Adv. Mater.* **2009**, *21* (6), 665−669.

(28) Yao, X.; Xu, L. A.; Jiang, L. Fabrication and Characterization of Superhydrophobic Surfaces with Dynamic Stability. *Adv. Funct. Mater.* **2010**, *20* (19), 3343−3349.

(29) Liu, T. Y.; Kim, C. J. Turning a surface superrepellent even to completely wetting liquids. *Science* **2014**, *346* (6213), 1096−1100.

(30) Teisala, H.; Geyer, F.; Haapanen, J.; Juuti, P.; Makela, J. M.; Vollmer, D.; Butt, H. J. Ultrafast Processing of Hierarchical Nanotexture for a Transparent Superamphiphobic Coating with Extremely Low Roll-Off Angle and High Impalement Pressure. *Adv. Mater.* **2018**, *30* (14), 1706529.

(31) Lv, X. D.; Jiao, Y. L.; Wu, S. Z.; Li, C. Z.; Zhang, Y. Y.; Li, J. W.; Hu, Y. L.; Wu, D. Anisotropic Sliding of Underwater Bubbles On Microgrooved Slippery Surfaces by One-Step Femtosecond Laser Scanning. *ACS Appl. Mater. Interfaces* **2019**, *11* (22), 20574−20580.

(32) Zhang, Y. C.; Li, Y.; Hu, Y. L.; Zhu, X. L.; Huang, Y. W.; Zhang, Z.; Rao, S. L.; Hu, Z. J.; Qiu, W. X.; Wang, Y. L.; Li, G. Q.; Yang, L.; Li, J. W.; Wu, D.; Huang, W. H.; Qiu, C. W.; Chu, J. R. Localized Self- Growth of Reconfigurable Architectures Induced by a Femtosecond Laser on a Shape-Memory Polymer. *Adv. Mater.* **2018**, *30* (49), 1803072.

(33) Jiao, Y. L.; Li, C. Z.; Wu, S. Z.; Hu, Y. L.; Li, J. W.; Yang, L.; Wu, D.; Chu, J. R. Switchable Underwater Bubble Wettability on Laser-Induced Titanium Multiscale Micro-/Nanostructures by Vertically Crossed Scanning. *ACS Appl. Mater. Interfaces* **2018**, *10* (19), 16867−16873.

(34) Cassie, A. B. D.; Baxter, S. Wettability of porous surfaces. *Trans. Faraday Soc.* **1944**, *40*, 546−550.

(35) Quere, D. Wetting and roughness. *Annu. Rev. Mater. Res.* **2008**, *38*, 71−99.

(36) Extrand, C. W. Model for contact angles and hysteresis on rough and ultraphobic surfaces. *Langmuir* **2002**, *18* (21), 7991−7999.

(37) Choi, W.; Tuteja, A.; Chhatre, S.; Mabry, J. M.; Cohen, R. E.; McKinley, G. H. Fabrics with Tunable Oleophobicity. *Adv. Mater.* **2009**, *21* (21), 2190−2195.

(38) Lafuma, A.; Quere, D. Superhydrophobic states. *Nat. Mater.* **2003**, *2* (7), 457−460.

(39) Campos, R.; Guenthner, A. J.; Meuler, A. J.; Tuteja, A.; Cohen, R. E.; McKinley, G. H.; Haddad, T. S.; Mabry, J. M. Superoleophobic Surfaces through Control of Sprayed-on Stochastic Topography. *Langmuir* **2012**, *28* (25), 9834−9841.

(40) Lee, W. L.; Low, H. Y. Geometry- and Length Scale-Dependent Deformation and Recovery on Micro- and Nanopatterned Shape Memory Polymer Surfaces. *Sci. Rep.* **2016**, *6*, 23686.

(41) Butt, H. J.; Semprebon, C.; Papadopoulos, P.; Vollmer, D.; Brinkmann, M.; Ciccotti, M. Design principles for superamphiphobic surfaces. *Soft Matter* **2013**, *9* (2), 418−428.

(42) Voce, E. The relationship between stress and strain for homogeneous deformation, 1948.

(43) Extrand, C. W. Designing for optimum liquid repellency. *Langmuir* **2006**, *22* (4), 1711−1714.